Research Square

Preprints are preliminary reports that have not undergone peer review.
They should not be considered conclusive, used to inform clinical practice,
or referenced by the media as validated information.

Flood Detection and Cropland Damage Assessment Using Sentinel-1 SAR Time Series Multi-Source EO Data in the Sebou Basin, El Gharb plain, Morocco

Mariame CHAHBI

mariame.chahbi@uir.ac.ma

International University of Rabat

Marzia GABRIELE

Politecnico di Milano

Maryam MAZOUZ

International University of Rabat

Youssef ELGANADI

International University of Rabat

Research Article

Keywords: Sentinel-1 SAR, Flood mapping, Agricultural damage, Kenitra, Sidi Kacem, Sidi Sliman, Flood vulnerability, Remote sensing, Sebou basin

Posted Date: August 27th, 2026

DOI: https://doi.org/10.21203/rs.3.rs-10394650/v1

License: This work is licensed under a Creative Commons Attribution 4.0 International License.
Read Full License

Additional Declarations: No competing interests reported.

Research Article

Flood Detection and Cropland Damage Assessment Using Sentinel-1 SAR Time Series Multi-Source EO Data in the Sebou Basin, El Gharb plain, Morocco

Mariame CHAHBI [1]*, Marzia GABRIELE[2]*, Maryam MAZOUZ[1,3], Youssef ELGANADI[1]

[1] International University of Rabat, Urban Innovation and Heritage Lab, Morocco
[2] Politecnico di Milano, Department of Architecture, Built Environment and Construction Engineering, Milan, Italy
[3] Scientific Institute, Mohammed V University, Rabat, Morocco

Correspondence: mariame.chahbi@uir.ac.ma

**** These authors contributed equally and share first authorship.***

Abstract

Flooding is a recurrent hazard in the Sebou Basin, particularly across the agriculturally productive El Gharb plain, where it poses significant risks to cropland and regional food security. This study presents a multi-temporal flood detection and cropland damage assessment approach using Sentinel-1 Synthetic Aperture Radar (SAR) time series data, integrating both VV and VH polarizations to improve the reliability of inundation mapping under all weather conditions. The methodology is based on the analysis of temporal backscatter dynamics and anomaly detection, where deviations from baseline conditions are used to identify flooded areas. Negative anomalies in both VV and VH signals are exploited to capture the characteristic decrease in backscatter associated with open water surfaces, while reducing misclassification in vegetated and rough terrain. This approach avoids global thresholding methods and instead relies on pixel-wise temporal statistics for enhanced flood detection. Cropland areas are derived from the ESRI land Cover dataset 2024 (ArcGIS Living Atlas). The integration of flood extent maps with cropland mask enables a detailed assessment of the spatial distribution and extent of flood-affected agricultural areas.

Flood damage was most severe in low-lying zones and on bare or sparsely vegetated soils, where limited surface cover accelerates inundation. The SAR-based approach proved effective for operational flood monitoring and cropland damage assessment in the Sebou Basin. Results point to concrete priorities for risk management in the El Gharb plain: water retention infrastructure, soil conservation practices, and land use planning that explicitly accounts for flood recurrence in intensively cultivated lowlands.

Keywords: Sentinel-1 SAR; Flood mapping; Agricultural damage; Kenitra, Sidi Kacem, Sidi Sliman; Flood vulnerability; Remote sensing, Sebou basin.

1. Introduction

Flooding is among the most destructive natural hazards affecting agricultural systems worldwide, causing substantial economic losses, soil degradation, and disruptions to food production systems (Kassaw & Nebere, 2025; Rahman & Di, 2020) In Morocco, the Sebou Basin is one of the country's most agriculturally productive regions, with the El Gharb plain supplying a significant share of national cereal and citrus output. The plain's flat alluvial topography and expansion of cropland into natural floodplains have made it progressively more exposed to flood damage. Real-time monitoring is difficult with optical sensors, which lose coverage under the cloud conditions that typically accompany storm events, and there has been no systematic spatial framework for damage assessment. Combining high-resolution land-cover data with Synthetic Aperture Radar (SAR) observations offers a way to quantify flood impacts on Moroccan agriculture where conventional approaches fall short

The El Gharb plain is a low-lying alluvial system characterized by fine sediments, shallow slopes, and an extensive irrigation network. These conditions favor water accumulation and limit drainage capacity during periods of intense rainfall. Flood events are often triggered by prolonged precipitation combined with soil saturation, leading to surface runoff and river overflow. Optical remote sensing fails precisely when flood mapping is most needed: cloud cover during storm events blocks usable imagery. Sentinel-1 SAR images through clouds and at night, making it well-suited to active flood conditions.

SAR-based flood detection relies on the physical interaction between microwave signals and surface properties. Open water surfaces produce low backscatters due to specular reflection, while rough or vegetated surfaces generate higher returns. However, distinguishing flooded areas in agricultural landscapes remains challenging due to variability in vegetation

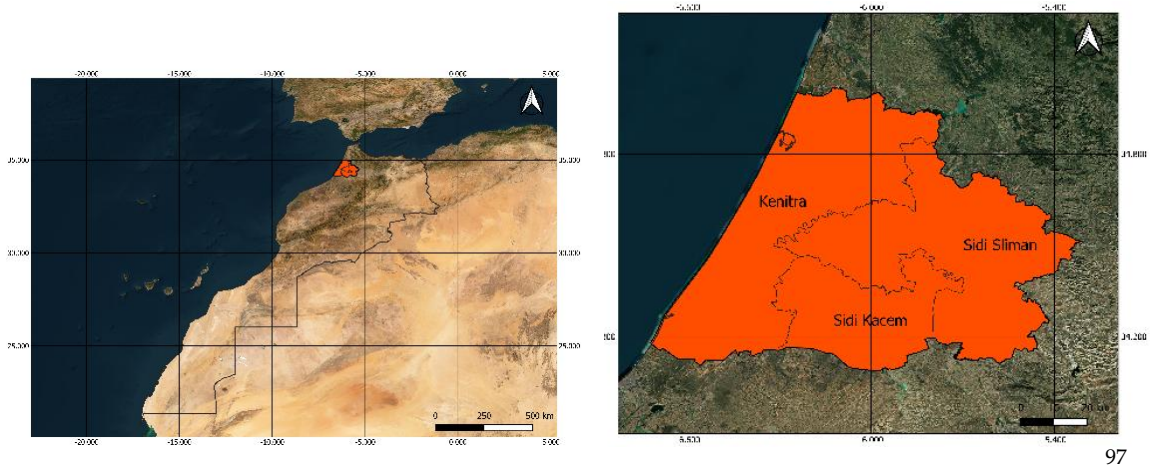
structure and soil moisture. Multi-temporal anomaly detection has become the standard for SAR-based flood mapping: per-pixel temporal statistics establish a backscatter baseline, and deviations flag inundation candidates. This study applies that principle to the Sebou Basin, pairing dual-polarization SAR change detection with ESRI Land Cover masking to map flood extent and estimate damage to cropland.

Synthetic Aperture Radar (SAR) systems, such as Sentinel-1, have become essential for flood monitoring due to their all-weather and day-night imaging capabilities. SAR backscatter is highly sensitive to surface water presence, making it suitable for flood detection even under cloud cover conditions. Numerous studies have demonstrated the effectiveness of Sentinel-1 VH and VV polarizations for flood mapping, with VH often providing stronger sensitivity to inundation due to vegetation-water interactions. However, challenges remain in distinguishing flood signals from low backscatter surfaces such as bare soil or smooth agricultural fields. To address these limitations, this study integrates SAR-based change detection, optical vegetation indices, and topographic filtering within a cloud-based geospatial framework. The objective is to (i) map flood extent using Sentinel-1 data, (ii) improve detection robustness using VH-dominant indices, and (iii) quantify flood impact on cropland areas in the Kenitra, Sidi Kacem, Sidi Sliman (KSS) provinces in Morocco.

2. Materials and Methods

2.1 Study Area

The KSS provinces (Kenitra, Sidi Kacem, and Sidi Slimane) lie in northwestern Morocco within the Rabat–Salé–Kenitra region. The area sits within the Gharb plain, a low-lying alluvial basin drained by the Sebou River, with flat topography, gentle slopes, and elevations ranging from near sea level to about 200 m at the inland margins. The combination of flat relief, extensive irrigated agriculture, and seasonal winter rainfall makes the plain flood-prone during wet periods. Climate is Mediterranean: mild, wet winters and hot, dry summers, with average annual precipitation between 300 and 500 mm. The study area spans approximately latitudes 34.0°N–35.0°N and longitudes 5.0°W–6.5°W. The three provinces together account for a substantial share of national cereal and citrus output, with large areas under wheat, olives, and irrigated crops. Figure 1 (a), (b) shows the geographic location of the study area within Morocco and the spatial extent of the selected provinces, highlighting the administrative boundaries and main hydrographic network.



(a) (b)

Figure 1. (a) Geographical Location of KSS Provinces within the Moroccan Territory. (b) Geographic boundaries of the provinces of KSS provinces, based on ESRI satellite images visualized in QGIS

The winter 2025-2026 was characterized by severe hydrometeorological disturbances in Morocco, driven by a succession of deep Atlantic cold depressions that produced prolonged and intense rainfall. These events triggered widespread flooding across low-lying plains and downstream river sectors, with the Gharb region and the Sebou plain among the most heavily impacted areas. As shown in Figure 2, extensive cropland was submerged under floodwaters, causing considerable damage to winter crops and highlighting the high vulnerability of this agriculturally strategic region to extreme hydroclimatic events.



(a) (b) (c)

Figure 2. (a), (b), (c) Aerial photographs documenting flood events across the Kenitra provinces, acquired by the author on 7 February 2026, showing visible surface water inundation in affected areas.

2.2 Data sources

The study relied on a combination of multi-sensor satellite imagery and ancillary geospatial datasets to analyze flood extent, dynamics, and impacts on agricultural areas within the KSS region, Morocco. Multi-temporal Sentinel-1 C-band Synthetic Aperture Radar (SAR) imagery (VV and VH polarizations) was used to detect floodwater under all-weather conditions and to capture pre-flood, peak-flood, and post-flood states. All datasets were processed in Google Earth Engine (GEE). Data sets include:

- **ESRI Land Cover 2024** (Sentinel-2 10 m Land Use/Land Cover Time Series): Used as the baseline land cover product derived from multi-temporal Sentinel-2 imagery using deep learning. The dataset provides annual global land cover maps at 10 m resolution, from which the "crops" class was extracted for cropland delineation and land use characterization.
- **Digital Elevation Model (SRTM DEM, 30 m):** Provided elevation and slope information to analyze water accumulation zones and surface flow direction.
- **Global Precipitation Measurement (GPM IMERG):** Satellite-based precipitation dataset. Weekly totals were compared across pre-event, peak-event, and post-event windows to identify the antecedent wet period that likely saturated soils before the main event, and to track how quickly rainfall declined during flood recession.
- **Provincial and commune boundary shapefiles (Morocco):** Official administrative datasets used to delineate the study area and quantify exposed agricultural land and flood-affected zones.

All satellite imagery used in this study is publicly available via Copernicus Open Access Hub (Sentinel-1: [S1A/S1B acquisitions], Sentinel-2: [S2A/S2B acquisitions]). Processed datasets and derived indices will be made available upon request and deposited in an open-access repository prior to publication.

2.3 Methods

A multi-stage flood detection framework was implemented combining SAR change detection, VH-weighted flood indexing, terrain filtering, and cropland exposure analysis. This study proposes a multi-source remote sensing framework for flood detection and cropland exposure assessment in the KSS provinces Morocco, using Sentinel-1 Synthetic Aperture Radar (SAR) time series by comparing pre- and post-event backscatter (VV and VH polarizations), enhanced through normalized change detection and a VH-weighted flood index to improve sensitivity to surface inundation., Sentinel-2 optical imagery, ESRI Land Cover data , and SRTM digital elevation data within the Google Earth Engine (GEE) platform. A terrain mask based on slope and elevation from the SRTM digital elevation model is applied to reduce false detections in non-flood-prone areas. A VH-dominant flood index based on SAR backscatter change detection is developed to identify inundated areas during a flood event in the KSS provinces, Morocco. Terrain constraints derived from slope and elevation are integrated to reduce false detections. Flood impacts on agriculture are quantified through spatial intersection with cropland masks and validated using Vegetation response through NDVI changes derived from Sentinel-2 imagery between pre- and post-flood periods, allowing assessment of crop condition changes within inundated zones. Results demonstrate that VH polarization is highly sensitive to flood conditions, and the proposed method effectively delineates flood extent and associated cropland exposure. flooded areas and affected cropland extent by intersecting the resulting cropland mask with the detected flood extent to extract flooded agricultural areas. and are quantified in hectares, providing a comprehensive spatial and quantitative assessment of flood impacts on agricultural systems. The framework provides a scalable and transferable approach for near-real-time flood monitoring and agricultural risk assessment.

2.3.1 Definition of pre- and post-flood periods using GPM IMERG

Pre-flood and post-flood hydro-meteorological conditions were characterized using the NASA Global Precipitation Measurement (GPM) IMERG V07 dataset, which provides satellite-based precipitation estimates at a spatial resolution

of ~0.1° and a temporal resolution of 30 minutes. The variable used in this study is precipitation (mm/hr), which was aggregated over defined temporal windows.

To capture the temporal evolution of rainfall associated with flood generation, the study period was divided into nine consecutive weekly intervals. These intervals were selected to represent antecedent rainfall conditions, peak precipitation phases, and post-event hydrological response.

For each period, cumulative precipitation was computed by temporal aggregation of IMERG observations as:

$$P_T = \sum_{t=1}^{n} p(t)$$

where P_T is the total precipitation for each period and $p(t)$ represents instantaneous rainfall rate.

2.3.2 Cropland Extraction

Cropland areas were extracted from the Esri Land Cover (2024) dataset, using the "crops" class derived from the Sentinel-2 10m land cover time series. This dataset provides global land cover information at 10m spatial resolution based on deep learning classification of multi-temporal Sentinel-2 imagery. Morphological filtering was applied to remove isolated pixels and improve spatial consistency of the resulting cropland mask.

2.3.3 SAR Data Processing and Change Detection

Pre-flood and flood-period Sentinel-1 composites were generated using median and minimum backscatter aggregation. Speckle noise was reduced using focal median filtering. Sentinel-1 Ground Range Detected (GRD) imagery was filtered by acquisition mode (IW), descending orbit, and dual polarization (VV and VH). Median composites were generated for pre-event and flood periods, while minimum backscatter during the flood period was used to capture peak inundation, following established SAR flood mapping approaches (Pulvirenti et al., 2011; Twele et al., 2016)

Backscatter change detection was performed using normalized differences to reduce spatial variability:

$$\Delta\sigma^0_{norm} = \frac{\sigma^0_{pre} - \sigma^0_{post}}{| \sigma^0_{pre} | + \epsilon}$$

where:

σ^0_{pre} : backscatter *before* the event

σ^0_{post}: backscatter *after* the event

$| \sigma^0_{pre} |$: absolute value (to avoid sign issues)

ϵ : very small number (to avoid division by zero)

This normalization improves robustness across heterogeneous land surfaces (Schumann & Moller, 2015)

2.3.4 Polarization Ratio Feature

To enhance flood detection sensitivity, a structural scattering descriptor was computed using the VH–VV polarization difference in decibel (dB) space:

$$R = I^{VH}_{post} - I^{VV}_{post}$$

This ratio improves discrimination between flooded vegetation, open water, and non-flooded surfaces by capturing relative scattering behavior between polarizations (Twele et al., 2016).

2.3.5 SAR-Based Flood Index and Otsu Adaptive Thresholding

Synthetic Aperture Radar (SAR) backscatter change was computed between pre-event and flood-period observations for both VV and VH polarizations:

$$VV_{drop} = VV_{pre} - VV_{post}$$
$$VH_{drop} = VH_{pre} - VH_{post}$$

To reduce the influence of baseline backscatter variability, normalized changes were calculated as:

$$VV_{norm} = \frac{VV_{drop}}{| VV_{pre} | + \epsilon}$$

$$VH_{norm} = \frac{VH_{drop}}{| VH_{pre} | + \epsilon}$$

where $\epsilon = 0.001$ prevents division by zero and ensures numerical stability.

A SAR-based flood index (FI) was then constructed by combining normalized VV and VH changes, with a higher weight assigned to VH polarization due to its stronger sensitivity to surface water and vegetation inundation (Henry et al., 2006):

$$FI = 0.2 \cdot VV_{norm} + 0.8 \cdot VH_{norm}$$

Instead of relying solely on fixed empirical thresholds, flood delineation was primarily performed using an adaptive threshold derived from Otsu's method. This method determines the optimal threshold by maximizing the between-class variance of the flood index histogram, enabling automatic separation of flooded and non-flooded pixels (Otsu, 1979)

The optimal threshold T_{Otsu} is defined as:

$$T_{Otsu} = \arg\max_{t}[\omega_1(t)\omega_2(t)(\mu_1(t) - \mu_2(t))^2]$$

where $\omega_1(t)$ and $\omega_2(t)$ are the probabilities of the two classes and $\mu_1(t)$, $\mu_2(t)$ are their corresponding means.

Flood pixels were classified using:

$$Flood = FI > T_{Otsu}$$

This adaptive formulation allows the threshold to adjust dynamically to scene-specific backscatter distributions and heterogeneous land cover conditions, improving generalization compared to static thresholding approaches. (Martinis et al., 2009; Pulvirenti et al., 2011, Uça Avcı et al., 2006)

2.3.6 Post-Processing and Topographic Filtering

Morphological filtering was applied to refine the flood mask, followed by topographic constraints using slope and elevation derived from the SRTM DEM. Areas with slopes greater than 5° and elevations above 120 m were excluded to reduce false detections in non-flood-prone areas. These conditions are consistent with hydrological behavior and commonly applied in SAR-based flood mapping (Tanguy et al., 2017). The final flood extent was obtained by combining the filtered classification with terrain masks, ensuring physically consistent flood delineation.

2.3.7 Flooded Cropland Mapping and Area Estimation

Flooded cropland was obtained by intersecting the final flood extent with the cropland mask derived from ESRI Land Cover dataset. This spatial overlay allows the identification of agricultural areas affected by inundations. The affected areas were quantified using pixel-based area aggregation, a standard approach in remote sensing-based flood impact assessment (Bauer-Marschallinger et al., 2022) Each pixel was converted into surface area using the native spatial resolution of the dataset (10 m × 10 m).

The total flooded area was computed in hectares as:

$$A_F = \sum_{x \in F} A_{pixel}$$

where:

$$A_{pixel} = 10 \times 10 = 100\, m^2$$

The total flooded area was computed in hectares as:

$$A_F^{ha} = \frac{A_F}{10^4}$$

where A_{pixel} represents the area of each flooded pixel in square meters, and 10^4 converts square meters to hectares.

Flooded cropland area was then derived by applying the same aggregation procedure on the masked intersection between the flood extent and cropland layer, enabling quantification of agricultural exposure to flooding.

$$F_c(x) = F(x) \cdot C(x)$$

Where:

- $F(x)$: flood extent
- $C(x)$: cropland mask

$$A_{F_c}^{ha} = \frac{\sum F_c(x) A_{pixel}}{10^4}$$

2.3.8 Histogram Based Statistical Validation

Probability distributions of VV, VH, and the VH-VV ratio were plotted as histograms to examine how clearly the three metrics separate flooded from non-flooded pixels. VH backscatter change shows two distinct modes: open water pixels cluster at large negative values, driven by specular reflection, while inundated vegetation pixels fall at smaller negative values where partial volume scattering limits the backscatter drop (Pulvirenti et al., 2011; Toma, Sandric, et al., 2024; Tsyganskaya et al., 2018). The VV channel demonstrates comparable inter-class separation at a reduced dynamic range, while the VH-VV ratio provides complementary structural discrimination, with strongly negative values (< −20

dB) indicative of specular open water surfaces (Yu et al., 2026). The two modes are well-separated enough for Otsu thresholding to place the cut-point reliably between them, and the same bimodal pattern appears in both VV and VH channels (Yu et al., 2026; Dhanabalan et al., 2021)

2.3.9 Cross-Sensor Corroboration Using Sentinel-2 NDVI

To corroborate the SAR-derived flood extent with independent optical evidence, Sentinel-2 NDVI composites were generated for pre- and post-event periods under low cloud conditions. Vegetation response was assessed by computing pixel-level NDVI differences over SAR-identified flooded areas.

NDVI differences were computed to assess vegetation response over flooded surfaces:

$$NDVI = \frac{B8 - B4}{B8 + B4}$$

NDVI differences from Sentinel-2 were used to validate vegetation stress:

$$\Delta NDVI = NDVI_{pre} - NDVI_{post}$$

NDVI is widely used as an indicator of vegetation stress(Chahbi, et al., 2025, Chahbi, El Ganadi, & Idrissi Gartoumi, 2025) and flood impacts, and spatial agreement between NDVI decline and SAR-detected inundation serves as cross-sensor corroboration rather than independent accuracy assessment (Pettorelli, 2013)

3. Results

Three datasets form the backbone of the analysis: GPM IMERG rainfall records to define the flood window, Sentinel-1 SAR imagery for flood mapping, and ESRI Land Cover (Class 5) (2024) for cropland delineation. Weekly precipitation statistics identify the peak inundation period; SAR backscatter change detection maps the flood extent; and spatial intersection with the cropland layer produces the final agricultural exposure estimates.

3.1 Definition of pre- and post-flood periods using GPM IMERG with weekly interval statistics

Table 1. Minimum, mean, and maximum precipitation (mm) per week, Dec 2025 to Feb 2026

#	Week start	Week end	Min (mm)	Max (mm)	Mean (mm)	Level
1	28/12/2025	03/01/2026	114.53	251.74	192.76	Low to Moderate
2	04/01/2026	10/01/2026	13.79	117.61	50.36	Low
3	**11/01/2026**	**17/01/2026**	**37.53**	**354.69**	**148.45**	**Moderate**
4	**18/01/2026**	**24/01/2026**	**82.39**	**301.45**	**173.57**	**Moderate**
5	**25/01/2026**	**31/01/2026**	**37.36**	**180.06**	**106.42**	**Moderate**
6	**01/02/2026**	**07/02/2026**	**100.09**	**543.68**	**317.33**	**High**
7	**08/02/2026**	**14/02/2026**	**42.04**	**270.62**	**114.25**	**Moderate**
8	15/02/2026	21/02/2026	0.00	6.08	0.31	Low
9	22/02/2026	28/02/2026	0.00	14.09	2.95	Low

The resulting rainfall fields were spatially averaged over the study area to produce a single representative value per week (Table 1). Comparing these weekly totals across pre-event, peak-event, and post-event windows shows how precipitation accumulated before the flood and declined during recession. The pre-flood period covers the antecedent phase when rainfall likely brought soil close to saturation; post-flood periods track the hydrological response after the inundation peak detected in Sentinel-1 SAR data.

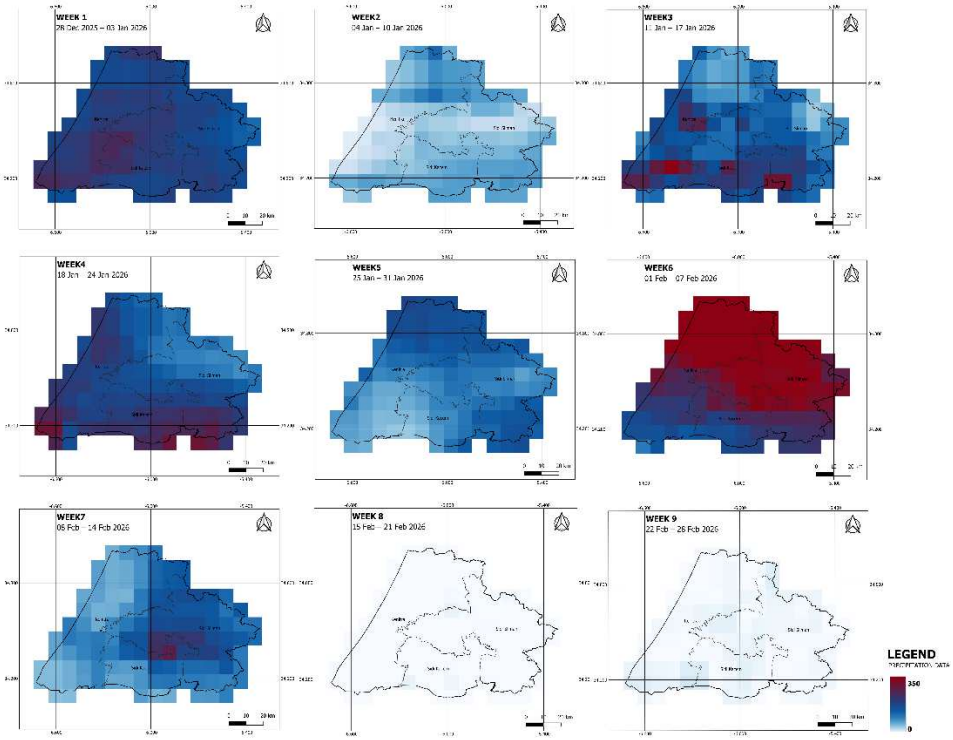


Figure 3. Meteorological rainfall (pluviometry) over the KSS provinces derived from GPM IMERG data computed in QGis, presented using weekly aggregated precipitation statistics to highlight temporal rainfall variability

The pre-flood period (Weeks 1 to 5) is characterized by sustained moderate to high rainfall (mean: 50–193 mm/week) (Figure 3). This sustained wet regime indicates progressive soil moisture accumulation and increasing catchment saturation, particularly during Weeks 3 to 5, which maintained mean values above 100mm. The flood event (Week 6) shows an extreme peak with a maximum value of 543.68 mm and a mean of 317.33 mm, representing the highest rainfall intensity in the entire study period. This abrupt increase following several wet weeks suggests a strong compound effect between antecedent soil moisture conditions and extreme rainfall, significantly enhancing flood generation potential. The post-flood period (Weeks 7 to 9) is marked by a sharp decline in precipitation, with near-zero values indicating hydrological recession and recovery.

3.2 Spatial Distribution of Flood Extent and Topographic Controls on Flood Distribution

Sentinel-1 SAR backscatter change detection mapped flood extent across the KSS region, with inundated pixels concentrated in the low-lying floodplain zones of the Sebou River. Adding VH-dominant weighting reduced speckle-related fragmentation relative to single-polarization mapping, producing more spatially coherent flood boundaries in mixed agricultural-fallow area

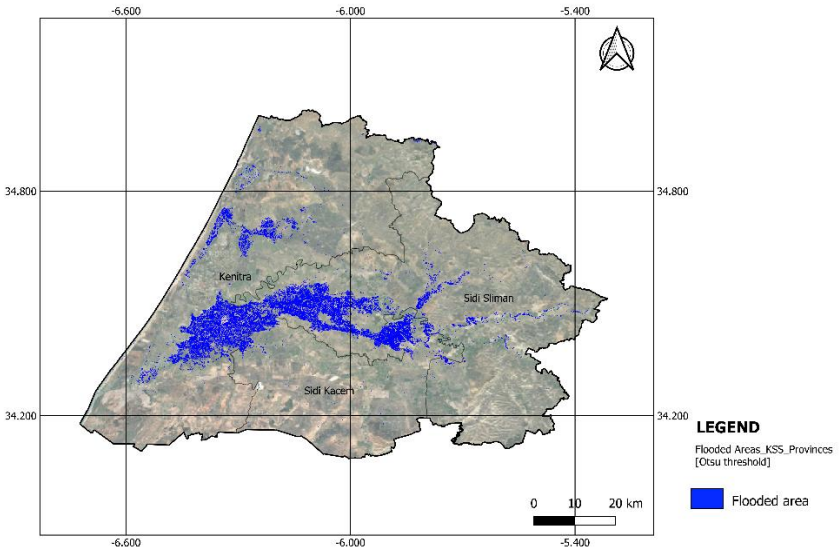


Figure 4. Spatial distribution of flooded areas across the Kenitra–Sidi Kacem–Sidi Slimane (KSS) provinces derived from Sentinel-1 SAR imagery using Otsu automatic thresholding. Processed in GEE and visualized in QGIS.

The Sentinel-1 SAR-derived flood map, processed in Google Earth Engine using Otsu automatic thresholding and visualized in QGIS, reveals extensive inundation across the Kenitra–Sidi Slimane–Sidi Kacem (KSS) provinces during the 2025–2026 winter flood episode. As shown in Figure 4, flooded areas are predominantly concentrated along the central lowland corridor of the Sebou plain, consistent with the flat alluvial topography and limited drainage capacity characteristic of the Gharb region. The total inundated area derived from the VH polarization channel reached approximately 207,112 ha, reflecting the exceptional magnitude of this event.

The Otsu thresholding algorithm yielded optimal backscatter separation thresholds of 4.74 dB (VV), 7.74 dB (VH), and −10.24 dB (VV/VH ratio), with the higher VH threshold confirming the superior sensitivity of cross-polarization backscatter to surface water presence in heterogeneous agricultural landscapes. This is consistent with findings reported in the literature, where VH polarization has demonstrated greater discriminative power for flood mapping in vegetated and cropland environments compared to single VV-based approaches (Fichtner et al., 2023; Twele et al., 2016).The elevated VH Otsu threshold, paired with a strongly negative ratio value, reflects the dominance of specular reflection over open water consistent with the expected physical behavior of smooth inundated surfaces. The VH-dominant flood index (0.8 VH, 0.2 VV) reduced false positives in bare soil areas, where low VV backscatter alone can mimic flood signatures when polarizations are weighted equally.

Terrain analysis revealed that more than 85% of detected flood pixels occurred in areas with slope < 5°, confirming the strong dependency of flood occurrence on low-gradient surfaces. Elevation constraints (<120 m) further eliminated misclassification in upland zones, demonstrating that integrating DEM-based filtering significantly improves SAR flood detection reliability.

3.3 Cropland flood impact assessment

Overlay analysis between the SAR-derived flood extent and the cropland mask revealed substantial agricultural exposure to inundation, with a total flooded cropland area of approximately **148,996 ha**, representing most of the total inundated surface across the KSS provinces (Figure5)

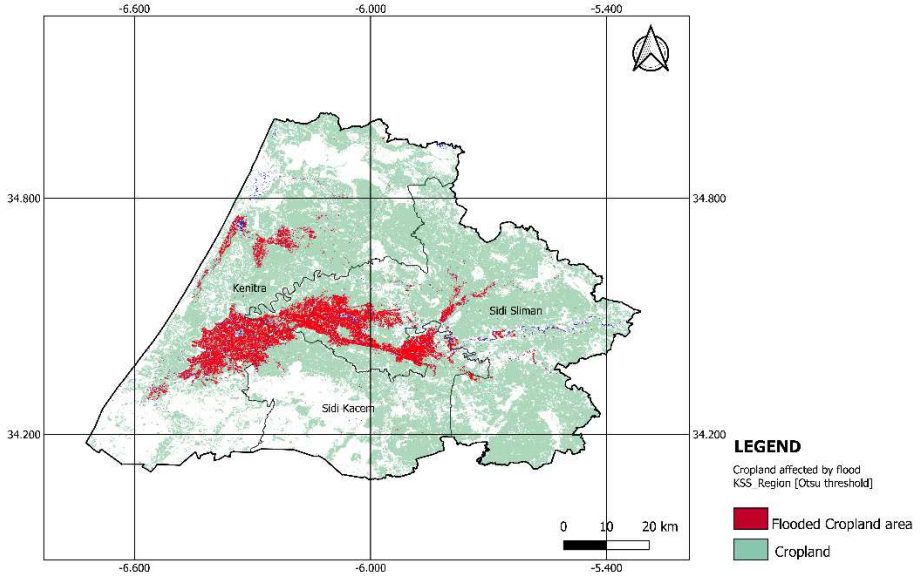
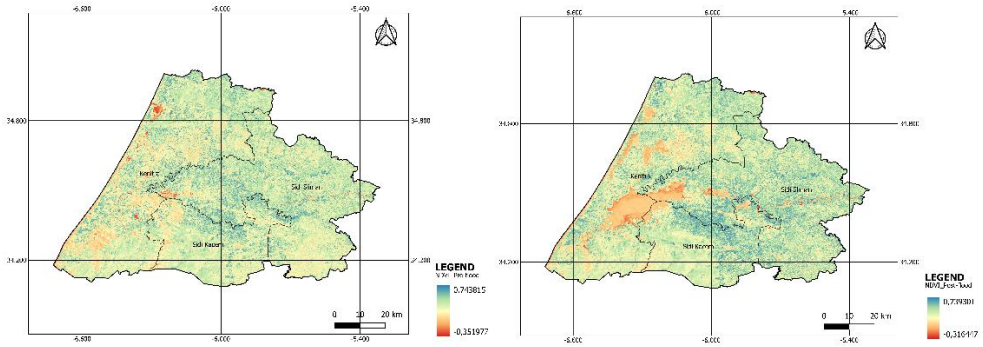


Figure 5. Spatial distribution of flooded cropland across the Kenitra–Sidi Kacem–Sidi Slimane (KSS) provinces derived from the overlay of Sentinel-1 SAR-based flood extent (Otsu thresholding) and ESRI Land Cover 2024 cropland mask (class 5). Processed in GEE and visualized in QGIS.

Flooded cropland concentrated in the valley-bottom fields along the Sebou plain- not scattered across the region, but in the low-gradient alluvial corridors where poorly drained soils and shallow water tables keep fields waterlogged well after peak inundation. This spatial pattern matters for risk management: the same zones flood repeatedly, which means SAR-derived flood frequency maps could directly inform where drainage investment is most needed and where crop insurance exposure is highest.

3.4 Vegetation Response and Cross-Sensor Corroboration

Sentinel-2 NDVI composites capture a spatial shift between the pre- and post-flood periods across the KSS floodplain: pre-flood values show moderate-to-high greenness across cropland; post-flood maps reveal a pronounced expansion of low NDVI concentrated along the Sebou inundation corridor (Figure 6), consistent with waterlogging-induced canopy stress in winter crops at early growth stages.



(a) (b)

Figure 6. (a) pre-flood NDVI; (b) post-flood NDVI, showing vegetation decline after the flood event. (b) both (a) and (b) are computed in Google Earth Engine and visualized in QGIS

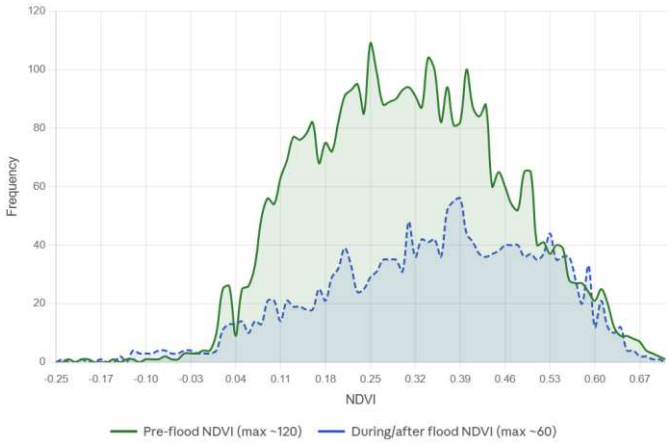


Figure 7. Pre- and Post-Flood NDVI Distribution Curves in Flooded Cropland computed in GEE.

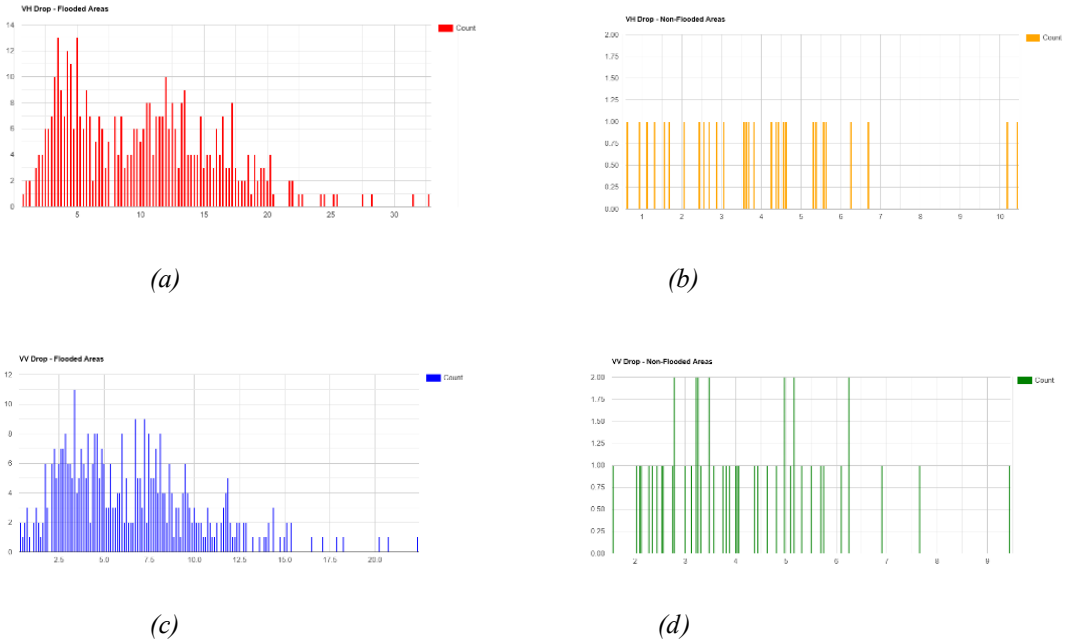
Both curves (Figure.7) use their actual raw frequency values on a shared y-axis capped at 120. The pre-flood curve naturally peaks around 109~120, while the post-flood curve stays within its original range of up to ~56, making the difference in sample density and distribution shape directly visible.

In the pre-flood composite (Figure 6a), vegetation cover is relatively uniform across cropland, with NDVI ranging from −0.35 to 0.74. The post-flood map (Figure 6b) shows a marked expansion of low NDVI values; warm orange-red tones; concentrated along the Sebou inundation corridor, indicating vegetation deterioration where SAR also detected flood presence.

Quantitatively, a mean NDVI drop of **0.059** was recorded over flooded surfaces, compared to a pre-flood mean NDVI of **0.040.** The spatial agreement between SAR-derived flood extent and NDVI-detected vegetation stress constitutes cross-sensor corroboration, not independent validation; neither dataset serves as ground truth for the other; but the convergence of radar and optical evidence reduces the likelihood that the mapped extent reflects SAR artefacts alone. The drop is modest in absolute terms, but its spatial coherence with the SAR-detected flood boundary is what matters: two sensors responding independently to the same physical event; surface water presence in SAR, reduced canopy greenness in optical; map the same footprint.

3.5 SAR-Based Flood Detection: Polarimetric Backscatter Analysis

Histograms of VH and VV backscatter change show clear separation between flooded and non-flooded pixels, with VH providing stronger discrimination against flooded pixels cluster at lower backscatter values driven by specular reflection over smooth water. (Figure 8).



(a) *(b)*

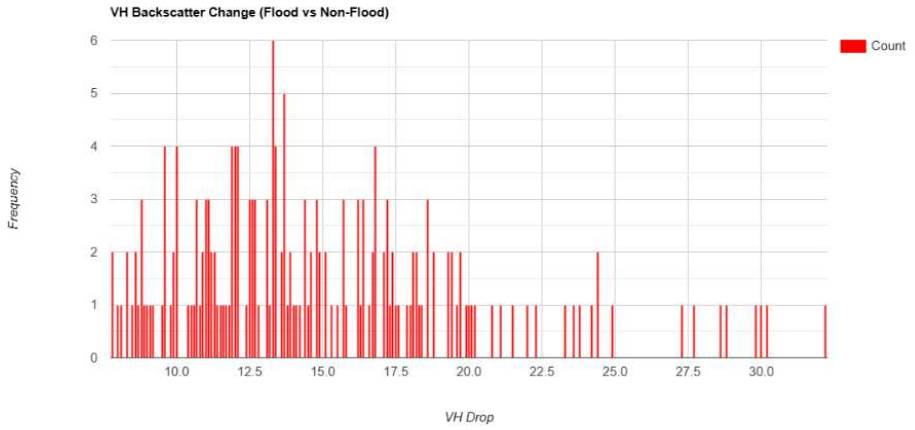
(c) *(d)*

Figure 8. (a) VH drop in flooded area, (b) VH drop in non-flooded area, (c) VV drop in flooded area, (d) VV drop in non-flooded area

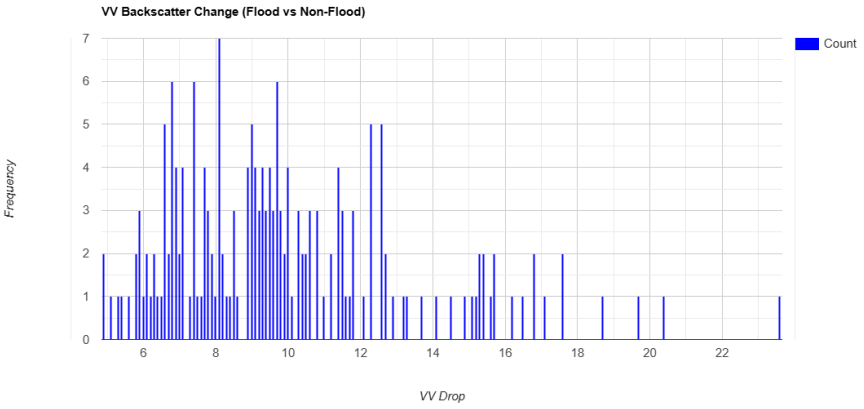
The VH backscatter distribution (Figure 8 a,b) is right-skewed, with the modal class near +2 dB and most pixels falling between 0 and 5 dB—low-to-moderate values consistent with flood-suppressed returns. A small left-side tail extends to roughly −5 dB, where backscatters increase slightly, likely reflecting heterogeneous cover or residual structural scattering. The minority of high-backscatter pixels at the right tail correspond to non-inundated or structurally complex surfaces.

3.5.1 VH Backscatter Change Between Flood and Non-Flood Areas

The histogram of VH backscatter change between flood and non-flood pixels (Figure 9(a)) reveals a strictly positive distribution spanning approximately 7 to 32 dB, with a modal value concentrated around 12–13 dB. The absence of zero or negative values across the entire sample confirms that flooded pixels consistently exhibit greater backscatter attenuation than their non-flooded counterparts under cross-polarized (VH) conditions. This result is consistent with the well-established physical mechanism of specular reflection over inundated surfaces, whereby smooth water bodies redirect incident microwave energy away from the sensor, resulting in substantially reduced backscatter returns relative to vegetated or rough terrain (Fichtner et al., 2023)



(a)



(b)

Figure 9. (a) VH backscatter change between flood and non-flood areas derived from Sentinel-1 SAR imagery, obtained via GEE. (b) VV backscatter change between flood and non-flood areas derived from Sentinel-1 SAR imagery (obtained via GEE)

The broad spread of the distribution (standard deviation estimated at ~4–5 dB) reflects the inherent heterogeneity of flood inundation conditions within the study area. Pixels exhibiting high VH differences (>20 dB) likely correspond to open water or deeply inundated agricultural land, where specular scattering dominates. In contrast, moderate difference values (7–15 dB) are more consistent with partially inundated vegetation or shallow floodwater overlying structured surfaces, where volume scattering contributions partially offset the specular signal attenuation (Giustarini et al., 2013). These findings suggest that a minimum VH backscatter difference threshold of approximately 7 dB can be reliably applied to discriminate flooded from non-flooded pixels in this dataset.

3.5.2 VV Backscatter Change Between Flood and Non-Flood Areas

The distribution of VV backscatter change between flood and non-flood pixels (Figure 9 (b) exhibits a strictly positive range spanning approximately 4 to 23 dB, with a primary mode at 7–8 dB and a secondary concentration of values near 12–13 dB, suggesting a broad-shouldered or weakly bimodal structure. As with the VH channel, the absence of zero or negative values confirms reliable discrimination between the two surface classes under co-polarized acquisition conditions. However, the overall magnitude of separation is measurably lower than that observed for VH, with the modal difference reduced by approximately 5 dB and the maximum observed value lower by approximately 9 dB.

This relative reduction in discriminative magnitude is consistent with established SAR theory. VV polarization is predominantly sensitive to surface dielectric properties and moisture content, rendering it less responsive to the geometric specular reflection mechanism that drives strong backscatter suppression over open water under VH (Martinis et al., 2018; Schlaffer et al., 2015) The bimodal tendency likely reflects two flood sub-classes; open water versus shallowly inundated vegetated surfaces; a distinction that future work could investigate by spatially stratifying pixels before analysis (Giustarini et al., 2013; Pulvirenti et al., 2011)

3.5.3 VH/VV Structural Ratio Distribution

The VH/VV polarization ratio, expressed as the difference VH − VV in logarithmic (dB) units, provides a structural characterization of surface scattering mechanisms independent of absolute backscatter magnitude. The observed distribution (Figure 10) spans a range of approximately −32 to −4 dB, with the bulk of the sample concentrated between −18 and −7 dB and a clear modal interval around −13 to −9 dB. All values are negative, as expected from the physical relationship between co- and cross-polarized backscatter, wherein VH returns are systematically lower than VV due to reduced depolarization from most natural surfaces.

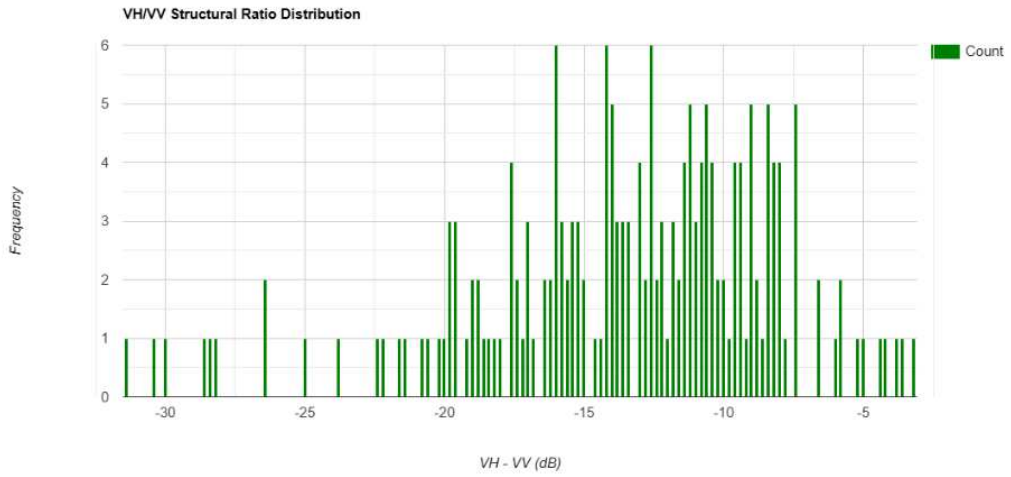


Figure 10. VH/VV polarization structural ratio distribution (VH − VV, dB) for flood-affected pixels derived from Sentinel-1 SAR imagery, obtained via GEE.

The distribution exhibits a pronounced left tail extending toward −32 dB, which is physically attributable to specular or quasi-specular scattering surfaces, most notably open water bodies and bare flooded soil where cross-polarized returns are dramatically suppressed relative to co-polarized returns. The central cluster between −15 and −8 dB is consistent with vegetated land covers and moderately rough surfaces, while values approaching −4 dB suggest the presence of double-bounce scattering structures, such as urban buildings or flooded tree stems acting as dihedral reflectors (Cazals et al., 2016; Tsyganskaya et al., 2018)

This polarimetric ratio therefore provides complementary discriminative information to absolute backscatter change metrics. Pixels with VH − VV < −20 dB can be considered strong candidates for open water inundation, while intermediate ratio values may indicate flooded vegetation or transitional land surface conditions. Incorporating this feature alongside absolute drop magnitudes enhances the physical interpretability of flood mapping outputs and reduces confusion between specular non-flood surfaces and genuine inundation**.**

3.5.4 Comparative Assessment of Polarimetric Flood Signatures

A synthesis of the three diagnostic distributions reveals a consistent and physically coherent pattern of flood-induced backscatter modification across both polarization channels**.** Table 2 summarizes the key discriminative statistics derived from the observed histograms.

Table 2. Comparative summary of VH and VV flood discrimination metrics.

Metric	VH Backscatter Change	VV Backscatter Change
Minimum observed difference	~7 dB	~4 dB
Modal difference	~12–13 dB	~7–8 dB
Maximum observed difference	~32 dB	~23 dB
Sign of all values	Strictly positive	Strictly positive
Relative discriminability	Higher	Moderate

The VH channel demonstrates superior flood discriminability across all metrics, with a modal separation approximately 5 dB greater than VV and a broader dynamic range extending to 32 dB. This finding corroborates the established preference for cross-polarized imagery in open-water flood mapping applications (Clement et al., 2018). The VH/VV structural ratio adds an independent dimension of physical interpretation, enabling surface type stratification within the flood-affected class and reducing potential confusion with specular non-flood surfaces such as calm water bodies or smooth bare soil in reference imagery (Toma, Șandric, et al., 2024).

Collectively, these results support the use of a multi-feature approach to flood classification, integrating VH backscatter change, VV backscatter change, and the VH/VV polarization ratio as complementary input variables. Such a feature combination is well-suited to supervised classification frameworks, including Support Vector Machines (SVM) and Random Forest algorithms, which have demonstrated robust performance in multi-polarization SAR flood detection tasks (Amer, 2025; Hansen et al., 2025; Irukumati et al., 2025).

4. Discussion

The results obtained for the Gharb plain confirm the effectiveness of Sentinel-1 SAR data for flood detection in lowland agricultural environments. The strong performance of VH polarization is consistent with recent studies showing its higher sensitivity to surface water and vegetation-water interactions compared to VV, particularly in heterogeneous croplands and irrigated systems (e.g., Pulvirenti et al., 2011; Twele et al., 2016)

The proposed SAR-based flood index, combined with Otsu adaptive thresholding, improved flood delineation under spatially variable land cover conditions. Recent literature highlights that adaptive histogram-based methods such as Otsu remain effective for SAR flood segmentation, especially in flat agricultural regions, although their performance can degrade in mixed or moisture-variable surfaces due to overlapping backscatter distributions (Ebadati et al., 2024; Liang & Liu, 2020; Tran et al., 2022; Zhuang et al., 2024). In this study, Otsu provided a data-driven threshold close to the empirically defined value, confirming the effectiveness of the proposed index while reducing dependence on manually tuned parameters. However, slight overestimation in low-backscatter agricultural fields suggests that statistical thresholding alone may still be influenced by soil moisture and post-harvest conditions, a limitation also reported in operational Sentinel-1 flood mapping studies(Toma, Șandric, et al., 2024; Wagner et al., 2025; Zhuang et al., 2024). This supports the need for hybrid approaches combining physical indices and adaptive statistics for more reliable flood delineation.

The NDVI shift over flooded areas; a mean drop of 0.059 across inundated cropland is consistent with short-term waterlogging stress in winter crops at early growth stage, and its spatial coincidence with the SAR flood footprint supports the cross-sensor coherence of the results.

Beyond crop loss, flooding in irrigated plains generates cascading costs. Drainage and pumping systems work harder after events, field recovery delays the next planting cycle, and waterlogged soils take weeks to regain trafficability. These secondary impacts are why near-real-time flood extent information matters for farm and water management decisions. Together, SAR change detection, VH-weighted indexing, Otsu thresholding, and terrain masking address the main failure modes of single-source flood mapping: cloud opacity, bare-soil false positives, and detections on steep slopes. The combination is well-matched to irrigated floodplains like the Gharb, where time-sensitive decisions follow quickly after flood events.

Land Surface Conditions and Flood Vulnerability: Strategies and Solutions

In agricultural plains such as the Gharb, bare soils prevalent during post-harvest periods exhibit reduced infiltration capacity, surface crusting, and accelerated runoff generation, all of which amplify flood peaks and extend inundation duration. Addressing these conditions requires strategies spanning from field scale to landscape governance. Water retention systems including retention ponds, check dams, and repurposed irrigation basins intercept excess runoff before it reaches main drainage channels, while simultaneously storing water that reduces energy intensive pumping during dry periods. Wetland restoration along the Sebou River tributaries would also reintroduce the natural flood buffering capacity that has progressively lost to agricultural intensification, delivering additional benefit in carbon sequestration and sediment regulation. At the field scale, soil cover and conservation practices; cover cropping, no-till farming, mulching, and residue retention; directly sustain infiltration rates and limit surface crusting, creating synergies between flood resilience and water use efficiency. At the governance level, floodplain zoning informed by SAR-derived flood frequency

maps can enable evidence based spatial planning, making intensive cropland away from high-risk zones and designating flood-prone areas for water compatible land uses.

These four strategies reinforce each other: water retention structures reduce the peak flows that SAR maps can track over time; soil cover practices slow the runoff that drives inundation; and floodplain zoning draws directly on SAR-derived flood frequency maps to assign risk classes to specific parcels in the Gharb plain.

5. Conclusion

This study demonstrates the effectiveness of Sentinel-1 SAR data for flood mapping in the Gharb agricultural plain using a physically based flood index combined with adaptive Otsu thresholding. The integration of VV and VH backscatter changes enabled effective detection of inundated areas, with VH polarization providing the strongest sensitivity to flood conditions. Terrain slope constraints and Sentinel-2 NDVI cross-sensor comparison supported the physical consistency of the flood extents and provided optical evidence of vegetation stress over inundated cropland.

Implemented in Google Earth Engine on freely available Sentinel-1 data, the framework produces flood extent maps and cropland exposure estimates within days of an event replicable across flood-prone basins through recalibration of terrain thresholds and the cropland mask. Policy efforts should prioritize: (i) integration of satellite-based flood monitoring into national agricultural risk management systems, (ii) reinforcement of drainage and irrigation infrastructure in flood-prone lowlands, and (iii) promotion of energy-efficient adaptive irrigation strategies to reduce post-flood recovery costs and (iiii) incorporation of remote sensing products into regional planning to support sustainable management of land water energy systems.

The workflow described here; open-access data, GEE processing, and freely available Sentinel-1 archives; makes it replicable in other flood-prone agricultural basins without institutional infrastructure. Future work should test the approach across multiple flood seasons to characterize interannual variability in crop damage and to calibrate drainage intervention priorities against observed yield loss.

Author Contributions: M.C. and M.G. contributed equally to the conceptualization, methodology development, and writing of this work. formal analysis, M.C.; investigation, M.C., M.G. and M.M.; data curation, M.C.; writing—original draft preparation, M.C. and M.G.; writing—review and editing, M.C. and M.G, M.M, Y.E.; visualization, M.C.; supervision, M.C.; project administration, M.C.; funding acquisition, not applicable. All authors have read and agreed to the published version of the manuscript.

Funding: This research was funded by the PNRR TNE EDU GPSEducation initiative (Politecnico di Milano, Milan). This research received no additional external funding

Data Availability Statement: The data supporting the findings of this study are available from the corresponding author upon reasonable request. No publicly archived dataset was generated during the current study.

Acknowledgments: The authors acknowledge institutional support from the PNRR TNE EDU GPSEducation initiative (Politecnico di Milano, Milan) and UIH Lab, UIR

The Web of Science Core Collection (Clarivate) was used as a research assistant tool for literature search, screening, and bibliographic support during the study. During the preparation of this manuscript, the authors used Claude AI for language refinement. The authors reviewed and edited all generated content and take full responsibility for the content of this publication.

All authors acknowledge the contributions of all collaborators involved in this work.

Conflicts of Interest: The authors declare no conflicts of interest.

REFERENCES

Amer, R. (2025). Machine Learning-Driven Rapid Flood Mapping for Tropical Storm Imelda Using Sentinel-1 SAR Imagery. *Remote Sensing*, *17*. https://doi.org/10.3390/rs17111869

Bauer-Marschallinger, B., Cao, S., Tupas, M. E., Roth, F., Navacchi, C., Melzer, T., Freeman, V., & Wagner, W. (2022). Satellite-Based Flood Mapping through Bayesian Inference from a Sentinel-1 SAR Datacube. *Remote Sensing*, *14*, 3673. https://doi.org/10.3390/rs14153673

Cazals, C., Rapinel, S., Frison, P.-L., Bonis, A., Mercier, G., Mallet, C., & Corgne, S. (2016). Mapping and Characterization of Hydrological Dynamics in a Coastal Marsh Using High Temporal Resolution Sentinel-1A Images. *Remote Sensing*, *8*, 570. https://doi.org/10.3390/rs8070570

Chahbi, M., El Ganadi, Y., & Idrissi Gartoumi, K. (2025). Monitoring urban vegetation by GeoAI driven multi-scale indices: A case study of Rabat, Morocco. *Journal of Umm Al-Qura University for Engineering and Architecture*, *16*(3), 649–663. https://doi.org/10.1007/s43995-025-00153-w

Chahbi, M., El Ganadi, Y., Idrissi Gartoumi, K., Moujoud, L., & Himeur, Z. (2025). Assessment of urban greening in fez, morocco: An integrated analysis combining remote sensing data analysis and urban policy review. *Journal of Umm Al-Qura University for Engineering and Architecture*, *16*(4), 1487–1498. https://doi.org/10.1007/s43995-025-00188-z

Clement, M. a., Kilsby, C. g., & Moore, P. (2018). Multi-temporal synthetic aperture radar flood mapping using change detection. *Journal of Flood Risk Management*, *11*(2), 152–168. https://doi.org/10.1111/jfr3.12303

Dhanabalan, S. P., Abdul Rahaman, S., & Jegankumar, R. (2021). FLOOD MONITORING USING SENTINEL-1 SAR DATA: A CASE STUDY BASED ON AN EVENT OF 2018 AND 2019 SOUTHERN PART OF KERALA. *The International Archives of the Photogrammetry, Remote Sensing and Spatial Information Sciences*, *XLIV-M-3–2021*, 37–41. ASPRS 2021 Annual Conference - 29 March–2 April 2021, virtual. https://doi.org/10.5194/isprs-archives-XLIV-M-3-2021-37-2021

Ebadati, B., Attarzadeh, R., Alikhani, M., Youssefi, F., & Pirasteh, S. (2024). Efficient Flood Detection through Hybrid Machine Learning and Metaheuristic Methods using Sentinel-1. *The International Archives of the Photogrammetry, Remote Sensing and Spatial Information Sciences*, *XLVIII-3/W3-2024*, 35–43. https://doi.org/10.5194/isprs-archives-XLVIII-3-W3-2024-35-2024

Fichtner, F., Mandery, N., Wieland, M., Groth, S., Martinis, S., & Riedlinger, T. (2023). Time-series analysis of Sentinel-1/2 data for flood detection using a discrete global grid system and seasonal decomposition. *International Journal of Applied Earth Observation and Geoinformation*, *119*, 103329. https://doi.org/10.1016/j.jag.2023.103329

Giustarini, L., Hostache, R., Matgen, P., Schumann, G. J.-P., Bates, P. D., & Mason, D. C. (2013). A Change Detection Approach to Flood Mapping in Urban Areas Using TerraSAR-X. *IEEE Transactions on Geoscience and Remote Sensing*, *51*(4), 2417–2430. https://doi.org/10.1109/TGRS.2012.2210901

Hansen, M., Vejby, J., & Koch, J. (2025). Flood mapping using Sentinel-1 imagery with topographical and hydrological contextualization: Case study from Ribe, Denmark. *International Journal of Applied Earth Observation and Geoinformation*, *143*, 104816. https://doi.org/10.1016/j.jag.2025.104816

Henry, J. -B., Chastanet, P., Fellah, K., & Desnos, Y. -L. (2006). Envisat multi-polarized ASAR data for flood mapping. *International Journal of Remote Sensing*, *27*(10), 1921–1929. https://doi.org/10.1080/01431160500486724

Irukumati, S., Vittal, A. R., & Gurunarayan, S. L. (2025). Comparative analysis of classification techniques for flood mapping using Sentinel 1 SAR data. *Environmental Earth Sciences*, *84*(14), 398. https://doi.org/10.1007/s12665-025-12381-3

Kassaw, D., & Nebere, A. (2025). Flood monitoring and damage assessment in agricultural field using Sentinel-1 SAR data in Gumara river catchment, Blue Nile basin. *Environmental Systems Research*, *14*(1), 32. https://doi.org/10.1186/s40068-025-00427-1

Liang, J., & Liu, D. (2020). A local thresholding approach to flood water delineation using Sentinel-1 SAR imagery. *ISPRS Journal of Photogrammetry and Remote Sensing*, *159*, 53–62. https://doi.org/10.1016/j.isprsjprs.2019.10.017

Martinis, S., Plank, S., & Ćwik, K. (2018). The Use of Sentinel-1 Time-Series Data to Improve Flood Monitoring in Arid Areas. *Remote Sensing*, *10*, 583. https://doi.org/10.3390/rs10040583

Martinis, S., Twele, A., & Voigt, S. (2009). Towards operational near real-time flood detection using a split-based automatic thresholding procedure on high resolution TerraSAR-X data. *Natural Hazards and Earth System Sciences*, *9*(2), 303–314. https://doi.org/10.5194/nhess-9-303-2009

Otsu, N. (1979). A Threshold Selection Method from Gray-Level Histograms. *IEEE Transactions on Systems, Man, and Cybernetics*, *9*(1), 62–66. https://doi.org/10.1109/TSMC.1979.4310076

Pettorelli, N. (2013). *The Normalized Difference Vegetation Index*. Oxford University Press. https://doi.org/10.1093/acprof:osobl/9780199693160.001.0001

Pulvirenti, L., Chini, M., Pierdicca, N., Guerriero, L., & Ferrazzoli, P. (2011). Flood monitoring using multi-temporal COSMO-SkyMed data: Image segmentation and signature interpretation. *Remote Sensing of Environment*, *115*(4), 990–1002. https://doi.org/10.1016/j.rse.2010.12.002

Rahman, M. S., & Di, L. (2020). A Systematic Review on Case Studies of Remote-Sensing-Based Flood Crop Loss Assessment. *Agriculture*, *10*(4), 131. https://doi.org/10.3390/agriculture10040131

Schlaffer, S., Matgen, P., Hollaus, M., & Wagner, W. (2015). Flood detection from multi-temporal SAR data using harmonic analysis and change detection. *International Journal of Applied Earth Observation and Geoinformation*, *38*, 15–24. https://doi.org/10.1016/j.jag.2014.12.001

Schumann, G. J.-P., & Moller, D. K. (2015). Microwave remote sensing of flood inundation. *Physics and Chemistry of the Earth, Parts A/B/C, Emerging Science and Applications with Microwave Remote Sensing Data*, *83–84*, 84–95. https://doi.org/10.1016/j.pce.2015.05.002

Tanguy, M., Chokmani, K., Bernier, M., Poulin, J., & Raymond, S. (2017). River flood mapping in urban areas combining Radarsat-2 data and flood return period data. *Remote Sensing of Environment*, *198*, 442–459. https://doi.org/10.1016/j.rse.2017.06.042

Toma, A., Sandric, I., & Mihai, B.-A. (2024). Flooded area detection and mapping from Sentinel-1 imagery. Complementary approaches and comparative performance evaluation. *European Journal of Remote Sensing*, *57*. https://doi.org/10.1080/22797254.2024.2414004

Toma, A., Șandric, I., & Mihai, B.-A. (2024). Flooded area detection and mapping from Sentinel-1 imagery. Complementary approaches and comparative performance evaluation. *European Journal of Remote Sensing*, *57*(1), 2414004. https://doi.org/10.1080/22797254.2024.2414004

Tran, K., Menenti, M., & Jia, L. (2022). Surface Water Mapping and Flood Monitoring in the Mekong Delta Using Sentinel-1 SAR Time Series and Otsu Threshold. *Remote Sensing*, *14*, 5721. https://doi.org/10.3390/rs14225721

Tsyganskaya, V., Martinis, S., Marzahn, P., & Ludwig, R. (2018). Detection of Temporary Flooded Vegetation Using Sentinel-1 Time Series Data. *Remote Sensing*, *10*, 1286. https://doi.org/10.3390/rs10081286

Twele, A., Cao, W., Plank, S., & Martinis, S. (2016). Sentinel-1-based flood mapping: A fully automated processing chain. *International Journal of Remote Sensing*, *37*, 2990–3004. https://doi.org/10.1080/01431161.2016.1192304

Uça Avcı, Z., Goral, B., Aktaş, A., & Sunar, F. (2006). *Flood Monitoring Using Multi-Temporal Radarsat-1 Images*.

Wagner, W., Bauer-Marschallinger, B., Roth, F., Stachl, T., Reimer, C., McCormick, N., Matgen, P., Chini, M., Li, Y., Martinis, S., Wieland, M., Kraft, F., Festa, D., Hassaan, M., Tupas, M. E., Zhao, J., Seewald, M., Riffler, M., Molini, L., … Salamon, P. (2025). *The Fully-Automatic Sentinel-1 Global Flood Monitoring Service: Scientific Challenges and Future Directions*. SSRN. https://doi.org/10.2139/ssrn.5110703

Yu, H., Xu, Y.-P., Huang, Y., & Chiang, Y.-M. (2026). Flood inundation monitoring with multi-source satellite imagery based on deep learning and explainable frameworks. *Journal of Hydrology*, *673*, 135409. https://doi.org/10.1016/j.jhydrol.2026.135409

Zhuang, H., Wang, P., Hao, M., Hongdong, F., & Tan, Z. (2024). Flood inundation mapping in SAR images based on nonlocal polarization combination features. *Journal of Hydrology*, *646*, 132326. https://doi.org/10.1016/j.jhydrol.2024.132326